



HAL
open science

The Composition of the South Polar Cap of Mars Derived From Orbital Data

A. Broquet, M. Wieczorek, W. Fa

► **To cite this version:**

A. Broquet, M. Wieczorek, W. Fa. The Composition of the South Polar Cap of Mars Derived From Orbital Data. *Journal of Geophysical Research. Planets*, 2021, 126 (8), 10.1029/2020JE006730 . hal-03365706

HAL Id: hal-03365706

<https://hal.science/hal-03365706>

Submitted on 8 Aug 2022

HAL is a multi-disciplinary open access archive for the deposit and dissemination of scientific research documents, whether they are published or not. The documents may come from teaching and research institutions in France or abroad, or from public or private research centers.

L'archive ouverte pluridisciplinaire **HAL**, est destinée au dépôt et à la diffusion de documents scientifiques de niveau recherche, publiés ou non, émanant des établissements d'enseignement et de recherche français ou étrangers, des laboratoires publics ou privés.

Copyright

The Composition of the South Polar Cap of Mars Derived From Orbital Data

 A. Broquet^{1,2} , M. A. Wieczorek¹ , and W. Fa^{3,4} 

¹Observatoire de la Côte d'Azur, CNRS, Laboratoire Lagrange, Université Côte d'Azur, Nice, France, ²Now at Lunar and Planetary Laboratory, University of Arizona, Tucson, AZ, USA, ³Institute of Remote Sensing and Geographical Information System, School of Earth and Space Sciences, Peking University, Beijing, China, ⁴State Key Laboratory of Lunar and Planetary Sciences, Macau University of Science and Technology, Macau, China

Key Points:

- Radar and gravity data are used to invert for the south polar cap composition and elastic thickness of the underlying lithosphere (T_e)
- T_e lower than at the north pole are allowed, which helps satisfy thermal evolution models that predict hemispheric heat flow patterns
- The polar cap is made mostly of H₂O and has more than the known 1 vol% CO₂ if the dust concentration is less than 9 vol%

Supporting Information:

Supporting Information may be found in the online version of this article.

Correspondence to:

A. Broquet,
adrien.broquet@oca.eu

Citation:

Broquet, A., Wieczorek, M. A., & Fa, W. (2021). The composition of the south polar cap of Mars derived from orbital data. *Journal of Geophysical Research: Planets*, 126, e2020JE006730. <https://doi.org/10.1029/2020JE006730>

Received 13 OCT 2020

Accepted 18 JUL 2021

Author Contributions:

Conceptualization: A. Broquet, M. A. Wieczorek, W. Fa

Formal analysis: A. Broquet, W. Fa

Funding acquisition: M. A. Wieczorek

Investigation: A. Broquet

Methodology: A. Broquet, W. Fa

Resources: M. A. Wieczorek

Software: A. Broquet

Supervision: M. A. Wieczorek, W. Fa

Validation: A. Broquet, M. A. Wieczorek, W. Fa

Writing – original draft: A. Broquet

Writing – review & editing: A. Broquet, M. A. Wieczorek, W. Fa

Broquet, M. A. Wieczorek, W. Fa

Abstract The flexure of the lithosphere under stresses imposed by the geologically young south polar cap is one of the few clues we have regarding the south polar cap composition and the present-day thermal state of Mars. Here, we combine radar, gravity, and topography data with a flexural loading model to estimate the bulk density (ρ) and average real dielectric constant (ϵ') of the south polar cap, and the elastic thickness of the lithosphere (T_e). Given the uncertainties of the data, our results constrain ρ to be 1,100–1,300 kg m⁻³ (best fit of 1,220 kg m⁻³), ϵ' to be 2.5–3.4 (best fit of 3.3), and T_e to be greater than 150 km (best fit of 360 km). Based on these results, the maximum lithospheric flexure is 770 m, and the polar cap volume could be up to 26% larger than previous estimates that did not account for lithospheric flexure. Our inferred compositions imply that the dust concentration would be at least 9 vol% if the CO₂ ice content were negligible, and that the CO₂ ice concentration would be more than the known 1 vol% CO₂ if the dust concentration were less than 9 vol%. The 1- σ lower limit on T_e implies a surface heat flow that is less than 23.5 mW m⁻². This lower limit is significantly less than the range of acceptable values at the north pole (330–450 km, heat flow of 11–16 mW m⁻²), and helps satisfy global thermal evolution simulations that predict hemispheric differences in surface heat flow.

Plain Language Summary The south polar cap of Mars is a tremendous reservoir of ices. It is transparent to radar wavelengths allowing us to probe its structure and composition. Here, we combine radar, gravity, and topography data with a flexural loading model to invert for the south polar cap composition and elastic thickness of the underlying lithosphere. We find that the lithosphere below the south pole is cold and strong, but with a rigidity that is potentially lower than at the north pole. The allowed range of lithospheric rigidities for the northern and southern lithospheres is compatible with hemispheric differences in heat flow of the planet predicted by thermal evolution models. The polar cap volume could be up to 26% higher than previous estimates that did not account for lithospheric flexure, which represents a significant quantity of trapped volatiles. Such as for the north pole, the south polar deposits are made mostly of water ice, and may have sequestered more CO₂ ice than has currently been detected depending on the assumed dust content. An independent estimate on the dust content would allow placing crucial constraints on the amount of CO₂ trapped in the south polar deposits.

1. Introduction

Mars harbors two geologically young (<100 Ma, Herkenhoff & Plaut, 2000; Koutnik et al., 2002) and large (~1,000 km across) ice caps at its north and south poles. Throughout millions of years of atmospheric circulation and variations of orbital parameters (Laskar et al., 2002), volatiles, and dust were partitioned among the polar regions, the atmosphere, and the regolith, which led to the formation of two antipodal, kilometers-thick, polar caps. As such, their deposits are a witness to the planet's recent climate and orbital evolution (Levrard et al., 2007). Like on Earth, where the composition of buried ices constrains climatic evolution (Lorius et al., 1985), knowing the composition of these tremendous reservoirs of ices and dust will help improve scenarios for the climate evolution of Mars.

The two polar caps further act as large-scale loads that can bend the crust and lithosphere (Broquet et al., 2020), and are likely the only million years old surface features on Mars that could generate a measurable deflection. Lacking in situ heat flow estimates, analysis of the lithospheric flexure beneath these two

polar caps is one of the only methods that give access to the present-day strength of the lithosphere, which is related to the thermal state of the planet (Ojha et al., 2021; Phillips et al., 2008) and the thickness of the crust and its heat production (Plesa et al., 2018; Thiriet et al., 2018).

A study by Broquet et al. (2020) has developed a technique that makes use of radar data and an elastic loading model to probe the composition of the north polar cap and elastic thickness of the underlying lithosphere. Using radar data from Mars Advanced Radar for Subsurface and Ionosphere Sounding (MARSIS; Picardi et al., 2005) and SHallow RADar (SHARAD; Seu et al., 2007), we have shown that the polar cap is made mostly of water ice, with up to 10 vol% CO₂ ice, depending on the dust content. The lithosphere was found to be thick and cold at the north pole, with an elastic thickness of 330–450 km and a surface heat flow of 11–16 mW m⁻² (see also Phillips et al., 2008). Whereas the long-wavelength (>400 km) gravity field does not correlate with the surface topography at the north pole (in part because of a poor resolution of the gravity models at high northern latitudes, see also Ojha et al., 2019), the south polar cap shows a clear gravitational signature. It is thus possible to use the gravity field as an additional constraint on the properties of the south polar cap and underlying lithosphere (Ding et al., 2019; Wieczorek, 2008; Zuber et al., 2007).

The outline of this study is as follows. First, we present our inversion approach to constrain the elastic thickness of the lithosphere, and the bulk density and dielectric constant of the south polar deposits using elevation, gravity, and MARSIS data. A similar approach was also used in Broquet et al. (2020), but one main difference, involving the definition of the pre-loading surface beneath the south polar cap, is here thoroughly discussed given that the southern highlands are considerably rougher than the northern lowlands. We next present the inversion results and discuss their implication for the composition and volume of the south polar cap and thermal state of the lithosphere.

2. Inversion Approach

We use the method of Broquet et al. (2020) to invert for the elastic thickness of the lithosphere (T_e), the average polar cap load density (ρ), and the average real part of the complex dielectric constant (ϵ' , hereafter abbreviated to dielectric constant) by minimizing the root-mean-square (rms) misfit of the function

$$\psi(\epsilon', T_e, \rho) = [h_e - h_0 - W(T_e, \rho)] - h_t(\epsilon'). \quad (1)$$

In this equation, h_e is surface elevation, h_0 is an estimated pre-loading surface topography before the polar cap formed, W is the computed deflection of the polar cap basement with respect to the pre-loading surface, and h_t is the thickness of the polar cap derived from radar data. All these terms depend implicitly on position. The first term in square brackets represents the thickness of the polar cap at a given location based on the surface elevation and lithospheric deflection and is dependent on the density of the polar cap and the elastic thickness. The last term is a measurement of the thickness of the polar cap from radar data, which depends on the assumed dielectric constant. The two terms of this equation are coupled in that the thickness of the polar cap determines the total load acting on the lithosphere and hence the amount of lithospheric flexure (W).

The elastic thickness, dielectric constant, and polar cap density are assumed to be laterally constant in our model, which is an assumption that has been employed in several previous studies (e.g., Khuller & Plaut, 2021; Plaut et al., 2007; Selvans et al., 2010). However, our misfit function accounts for the possibility of having lithospheric flexure ($T_e < \infty$) and has thus additional degrees of freedom compared to most previous studies where it was neglected (e.g., Grima et al., 2009; Khuller & Plaut, 2021). The inclusion of lateral variations in density and dielectric constant is not possible using the above misfit function and would require additional constraints. Later, in Sections 3 and 4, we will assess the possible effects of lateral variations in these parameters on our results. In the following three subsections, we discuss the main aspects of our inversion approach, which are the estimation of the pre-loading surface, the calculation of the lithospheric deflection with respect to this pre-loading surface, and the radar estimates of the thickness of the polar deposits.

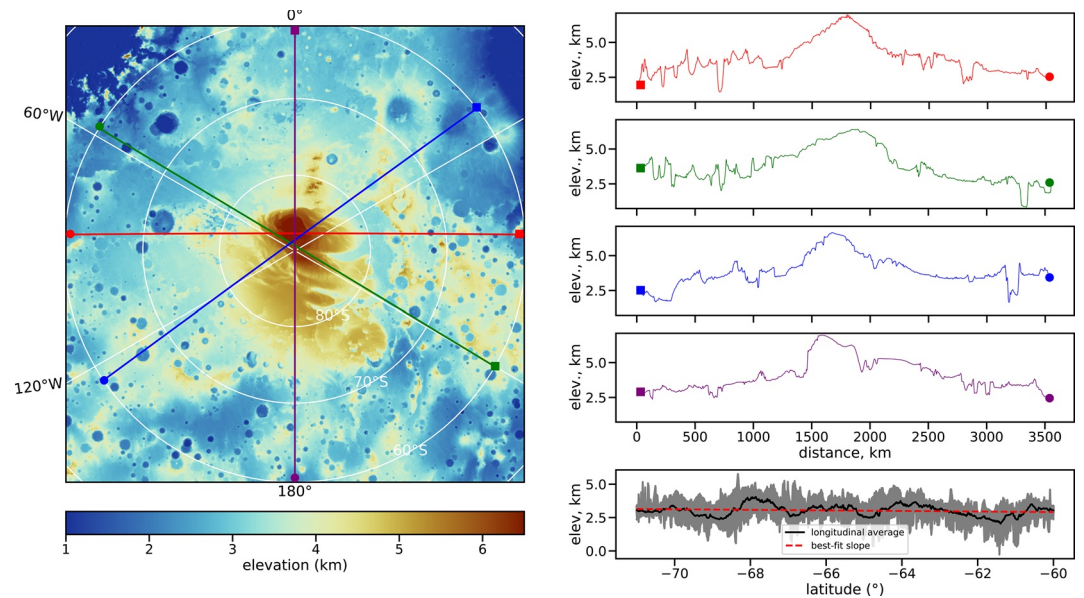


Figure 1. (Left) MOLA elevation map of the south polar cap of Mars with color-coded profiles used for plotting elevation profiles in the right panel. (Right) Extracted elevation profiles as a function of distance or latitude showing that there is no observable downward deflection associated with the load of the south polar cap. The bottom panel plots 100 example elevation profiles, equally spaced in longitude from 0 to 360° (gray), the elevation averaged over longitude (black), and the best-fitting linear slope (red) from 71°S to 60°S.

2.1. Pre-Loading Surface

The pre-loading surface (h_0) was obtained using a technique that is modified from Broquet et al. (2020) for the north polar cap. In that study, the elevation of the pre-loading surface was determined far from the edge of the north polar cap (about 900 km), and was then interpolated poleward beneath the polar cap. Given that the northern lowlands of Mars are relatively flat, it was straightforward in that study to estimate this surface with good accuracy. This technique, however, did not work as well for the south polar cap because the surface relief of the southern highlands is considerably more rugged than that of the northern lowlands. For example, over a 50 km length scale, the rms height of the southern highlands and northern lowlands is about 400 and 50 m, respectively, which represents a difference of a factor of 8. We will see later that one of the primary sources of uncertainty in our analysis is the uncertainty in our estimate of the pre-loading surface of the southern highlands.

In order to characterize the topography exterior to the polar cap, we show four different representative elevation profiles across the south polar deposits in Figure 1, along with an azimuthal average of the elevation. The south polar cap is seen to be highly asymmetric. Even though the average edge of the polar cap lies at about 700 km from the south pole, the polar cap extends in places to a distance of 1,100 km (71°S). For this reason, the azimuthally averaged profile in the lower right panel is plotted from 71°S to 60°S. As is seen, there is no detectable flexural signal in the surface topography exterior to the south polar cap, neither in the individual profiles nor in the azimuthally averaged profile. We demonstrate in Appendix A that it would, in fact, be unlikely to detect such a signal in an azimuthally averaged topographic profile given the natural variability in height of the surrounding highlands and the expected magnitude of the lithospheric flexure, which both are on the order of a few hundreds of meters. The lower right panel of Figure 1 also plots the best-fitting linear slope of the highlands between 71°S and 60°S, where the average elevation is found to increase slightly by about 21 m per degree latitude toward the pole. Even though a flexural signal would have predicted the elevation to decrease toward the pole, Appendix A also demonstrates that the small magnitude of the observed slope is consistent with what one would expect due to the natural surface roughness of the southern highlands.

Since there is no clear flexural signal in the highlands exterior of the south polar cap, we estimated the pre-loading surface using several different techniques (see Appendix B). For our preferred technique, we

simply interpolated poleward the elevation data near the edge of the cap itself, which was defined by the edge of the Amazonian polar undivided unit as mapped by Tanaka et al. (2014). Our interpolation method made use of the minimum curvature method of Smith and Wessel (1990) with a tension of 0.35, which is the recommended value for steep topography. The interpolated pre-loading surface is shown in the upper left panel of Figure 2. As opposed to using elevations further from the polar cap, this approach allowed us to avoid spurious and unrelated long-wavelength topographic signals associated with the rugged highlands. This estimate of the pre-loading surface will be used when presenting our results, unless otherwise stated.

In order to assess the uncertainty in the pre-loading surface and its influence on our results, we considered several different estimates that are described in more detail in Appendix B. First, by using the average elevation in a latitudinal band far from the polar cap, the pre-loading surface beneath the polar cap was found to be on average 560 m below our preferred case (Figure S1). This is the opposite of what one would expect if the polar cap flexed the lithosphere downward. Second, extrapolating the elevations in the same latitudinal bands toward the pole using a linear function gave rise to pre-loading surfaces that were about 200 m below our nominal case (Figure S1). For a third approach, we used a mask that was slightly modified from that of Tanaka et al. (2014) (Figure S2). Interpolation of the elevation data at the edge of this mask gave rise to a pre-loading surface about 300 m below our nominal case. Finally, we estimated the flexure at the edge of the polar cap using an elastic thickness of 90 km, which is the minimum allowed value from our gravity inversion that is discussed in Section 3 and that does not include any radar constraints (Figure S3). The predicted flexure at the edge of the polar unit for this elastic thickness is about 350 m, which would correspond to a pre-loading surface 350 m above our nominal case. Based on these results, we will assume that the height of the pre-loading surface is uncertain by ± 350 m.

2.2. Lithospheric Deflection

The elastic deflection of the lithosphere (W) was computed using the loading model presented in Broquet and Wiczorek (2019) and Broquet et al. (2020) (the relevant equations are provided in Appendix C). Importantly, lithospheric flexure will create long-wavelength relief at the base of the polar cap that is anti-correlated with the surface relief. The densities of the crust and mantle were set to 2,900 and 3,500 kg m^{-3} respectively, the crustal thickness (T_c) was set to 60 km (Neumann et al., 2004), Young's modulus (E) was set to 100 GPa, and Poisson's ratio (ν) was assumed to be 0.25, which are values used in most flexure models applied to Mars (e.g., McGovern et al., 2002; Phillips et al., 2008). We emphasize that it is important to make use of the same elastic parameters (E and ν) when comparing elastic thickness estimates with other studies. We also note that a variation of 200 kg m^{-3} for the crust or mantle densities, or a 30% variation in either E or ν would result in a less than 10% variation in T_c . Varying T_c has no significant impact on the flexure as this is a second-order term that is only used in the "self-gravity" correction (see Equation C7).

In a study by Goossens et al. (2017), the authors inverted for the density of crustal materials across the planet. In the southern hemisphere, the density of the crust was found to be about 1,800 kg m^{-3} . Though this might be an appropriate density for the upper few km of the crust, the gravity analysis of Goossens et al. (2017) was not capable of determining the depth range over which these densities applied as a result of the low-resolution of the Mars gravity models. To first order, the depth sensitivity of such analysis is given by the range of topographic elevations within the analysis regions, which is about 6 km. As such, the low-density obtained in Goossens et al. (2017) is not likely to be representative of the bulk crust in the southern hemisphere. Finally, we note that Goossens et al. (2017) did not report uncertainties for their density analyses, though these are likely to be large due to the weak correlation between gravity and topography, and the influence of lithospheric flexure at the investigated wavelengths.

2.3. Radar Thickness

The radar thickness (h_r) was derived from MARSIS data that have a range resolution in vacuum of 150 m (Picardi et al., 2005). We picked manually 1,000 locations that are spatially scattered across the polar deposits (Figure 2, upper right), investigated all available reduced MARSIS radargrams (Subsurface Sounding 3 data product, see Orosei et al., 2015), and identified visually the reflections arising from the icy surface and the ice-substratum interface at two frequency bands (3 and 4 MHz, see Figure S4).

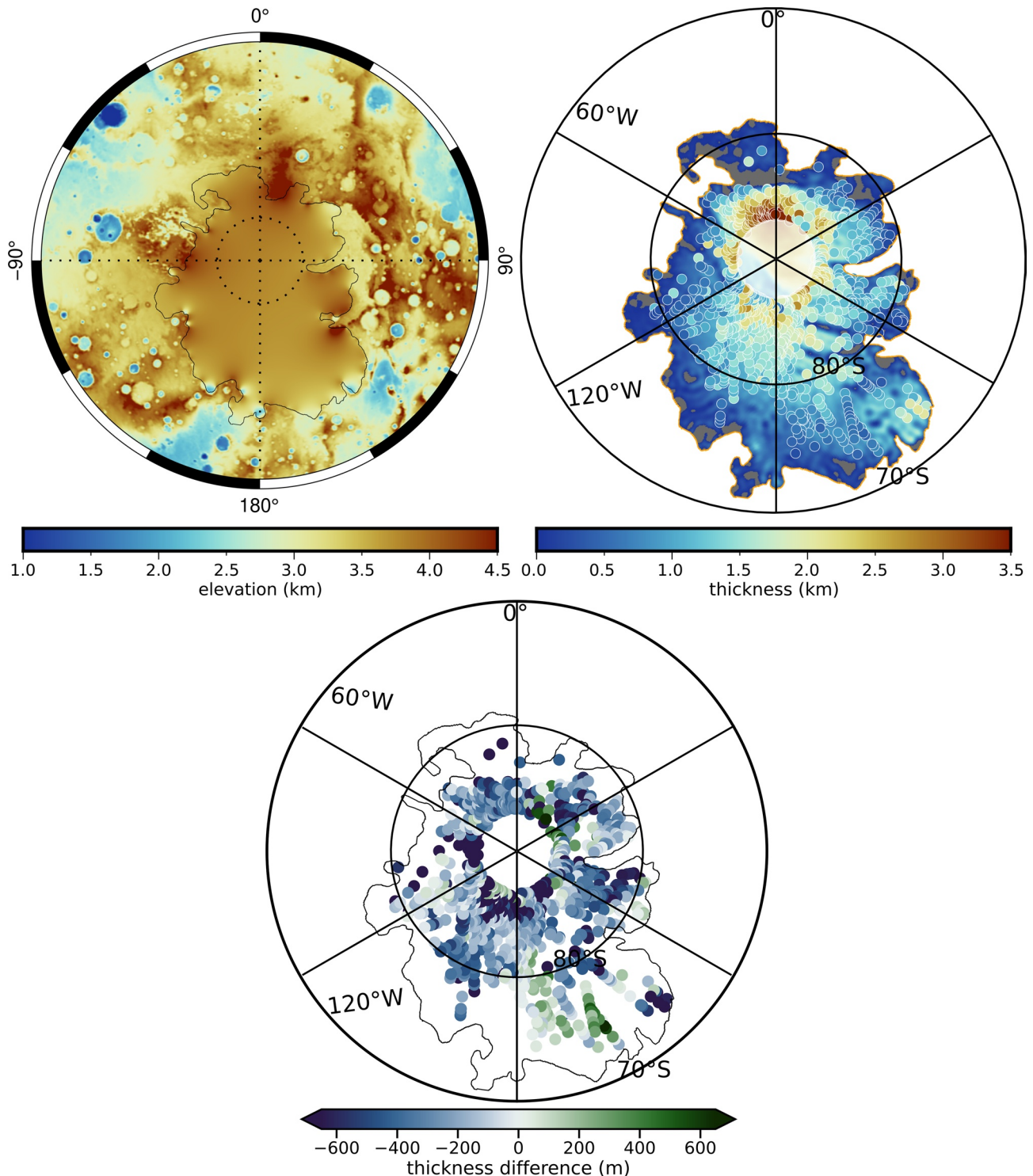


Figure 2. (Upper left) Pre-loading surface poleward of 65°S using elevation data at the edge of the Amazonian polar undivided unit given in Tanaka et al. (2014). (Upper right) Estimated thickness of the south polar cap from Mars Advanced Radar for Subsurface and Ionosphere Sounding (MARSIS) and MOLA surface elevations. The map shows the polar cap thickness from MOLA data under the assumption that the base of the polar cap follows the regional surface shown in the left image ($h_e - h_0$). The filled colored circles correspond to the thickness obtained at 1,000 regions from MARSIS radargrams (h_i) for $\epsilon' = 3.0$. The inner white circle poleward of 87°S masks the region where no radar data are available, and negative thicknesses (set to zero) are colored in gray. (Bottom) Difference between the estimated thickness of the south polar cap from MOLA surface elevations and MARSIS for $\epsilon' = 3.0$, which are on average -290 ± 350 m (MARSIS thicknesses are on average greater than MOLA thicknesses).

These reduced MARSIS radargrams have been previously processed using Doppler filtering techniques, which ensures that most surface off-nadir echoes (or clutter) have been removed (Orosei et al., 2015). The topography surrounding each measurement was further inspected in order to ensure that the region extending several Fresnel zones, which is about 23 km, was generally flat and that there were no steep scarps or canyons that could give rise to strong off-nadir surface returns. The surface reflectors were generally selected as those echoes with the strongest echo strength and with the shortest time delay, and the deepest subsurface reflectors were identified as the strongest echoes with the largest time delay (Figure S4). For each location, the lateral continuity (i.e., constant in time delay) of the surface and subsurface reflectors were verified to extend at least seven frames along the orbital track (corresponding to a horizontal distance of about 35 km). Using data from several orbital tracks and ensuring that the selected echoes are laterally continuous at a scale larger than the Fresnel zone of MARSIS allows avoiding interpreting off-nadir echoes (or clutter) as subsurface echoes, and spurious subcrustal reflectors as the polar cap basement. We also compared the radargrams with 20 simulated cluttergrams released by the MARSIS team in order to ensure that our picks were not affected by surface clutter.

The thickness of the polar deposits was calculated using the two-way time delay between the surface and subsurface echoes (t) and then converting the result into a distance by assuming a value for the dielectric constant

$$h_t = \frac{c t}{2\sqrt{\epsilon'}}, \quad (2)$$

where c is the speed of light in vacuum. It is clear from this equation that if the dielectric constant was chosen to be smaller than the true value, the inferred base of the polar cap would be deeper than expected, and hence anti-correlated with the surface relief. It is for this reason that we expect the presence of lithospheric flexure (which is anti-correlated with the long-wavelength surface relief) to influence our inversions for the dielectric constant. In particular, as the amount of lithospheric deflection increases (i.e., T_c decreases), the dielectric constant will need to decrease. We note that even if a small percentage of our picks of the basal surface were in error, being affected by surface clutter, the presence of thick CO₂ deposits, or the Dorsa Argentea Formation (Khuller & Plaut, 2021; Phillips et al., 2011), this would have only a small effect on the rms misfit function defined in Equation 1.

A map of the thickness of the south polar layered deposits was recently made available by Khuller and Plaut (2021), and we have found an overall good agreement with their measurements (Figure S5). Given that our radar picks were at slightly different locations, we compiled the difference in thickness for each of our points with the closest point in their analysis when the separation was less than 5 km (30% of our points had separation distances larger than this). The mean difference between the two data sets was only 30 m with a standard deviation of 250 m. Extending the 5 km distance comparison limit to 20 km allows for a comparison of 90% of our points and gives a difference of 15 ± 300 m. In both cases, the standard deviation is comparable to the natural variations in elevation of the surrounding highlands over a few kilometers length scales.

One difference between our mapping approach and that of Khuller and Plaut (2021) is that they excluded regions poleward of 84°S that contained a deep subsurface reflection that may correspond to the base of the Dorsa Argentea Formation. This formation is a dust-rich layer of glacial origin surrounding the south polar cap and that likely extends underneath the polar cap in places (Whitten et al., 2020). The Dorsa Argentea Formation is thought to be somewhat analogous to the basal unit beneath the north polar layered deposits (Nerozzi & Holt, 2019), and in a similar manner will also act as a load on the lithosphere. For our study, we thus made use of the deepest reflector that may correspond in some places to the base of this formation. About 70% of our radar picks that have a separation distance larger than 5 km with respect to those of Khuller and Plaut (2021) (about 200 points) are concentrated poleward of 84°S (Figure S5), where the Dorsa Argentea Formation is thought to be present. Nevertheless, when compared to the closest point (35 km distance on average), the differences are rarely more than 1 km (45 out of 1,000 points). Given the small number of radar picks that are potentially different, the rms misfit function defined in Equation 1 should not be significantly affected by a possible misidentification of the Dorsa Argentea Formation.

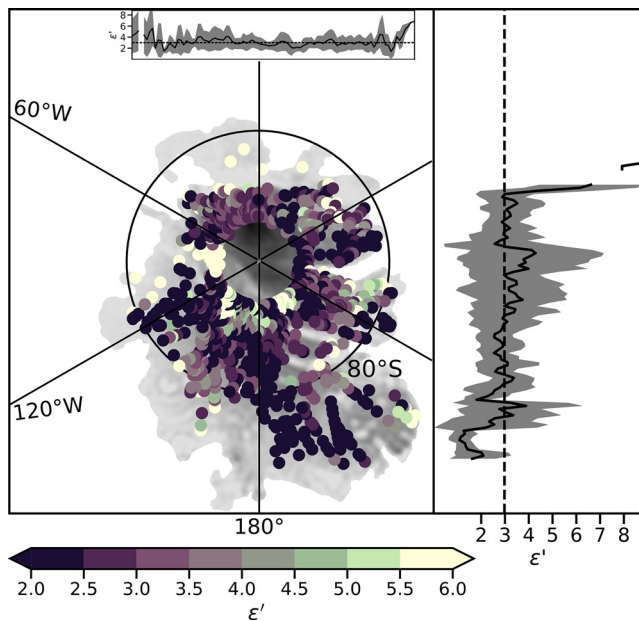


Figure 3. (Center image) Spatial variation of the dielectric constant (ϵ' , filled colored circles) under the assumption that the radar apparent measured thickness is equal to that using MOLA elevations with a slightly deformed basement corresponding to an elastic thickness of 250 km (see Equation 3). (Upper and right plots) Average dielectric constant (solid line) and standard deviation (shade) as a function of position using vertical (upper) and horizontal (right) profiles to extract the dielectric constant shown in the central image. Note that the uncertainties, such as that in the shape of the basal surface, are not accounted for in this plot.

In Figure 2 (upper right), we plot an estimated thickness of the south polar cap from MOLA surface elevations under the assumption that the base of the polar cap follows the pre-loading surface shown in the left image. We note that some regions at the edge of the polar deposits have a negative thickness, which is due to the elevation of the interpolated pre-loading basement exceeding the elevation of the deposits locally. On average, these negative thicknesses are only about 100 m, which is less than our 350 m uncertainty for the elevation of the pre-loading surface. For these isolated regions, which are concentrated where the polar cap is thinnest, we set the thickness of the polar deposits to zero and plotted the thickness as gray.

In this image, which neglects lithospheric flexure, the south polar cap has a maximum thickness of 3,240 m and an integrated volume of $1.29 \times 10^6 \text{ km}^3$, which are both consistent with the MARSIS derived estimates of Plaut et al. (2007) that obtained a thickness of $3.7 \pm 0.4 \text{ km}$ and a volume of $1.6 \pm 0.2 \times 10^6 \text{ km}^3$. Superposed on this map, we plot the polar cap thickness as determined by our 1,000 MARSIS measurements, with the fill color corresponding to the same color scale as the main image, for an assumed $\epsilon' = 3.0$. We note that there are no radar data poleward 87°S . The maximum thickness of the radar data is 3,590 m, which is also consistent with that obtained in Plaut et al. (2007) and Khuller and Plaut (2021). In the lower panel of this figure, we plot the difference between the MOLA and MARSIS thickness estimates for $\epsilon' = 3.0$. The differences are seen to range from about -600 to 600 m with an average of -290 ± 350 m, where the MARSIS thicknesses are on average slightly greater than those based solely on the MOLA data. These differences are likely due to lateral variations in dielectric constant that are not accounted for by our model, lithospheric deflection beneath the polar deposits (quantified in Section 3, see also Figure S6), and the actual base of the south polar cap being more complex than the interpolated harmonic surface.

In Figure 3, we show an example of the possible spatial variations in the dielectric constant that could exist in the polar cap. Each value was derived using the observed MARSIS two-way travel time and the assumption that the apparent measured thickness was equal to that using the MOLA surface elevations and a slightly flexed basement corresponding to an elastic thickness of 250 km with a load density of $1,150 \text{ kg m}^{-3}$. In this case, the dielectric constant is

$$\epsilon' = \left[\frac{c t}{2(h_e - h_0 - W)} \right]^2, \quad (3)$$

which shows that this parameter is sensitive to the shape of the chosen pre-loading surface and amount of lithospheric flexure. For reference, the dielectric constants of CO_2 ice, water ice, and dusty materials are about 2.2, 3.0–3.15, and 6.0–8.8, respectively (see Table 1), and we note that dielectric constants less than 1.0 are meaningless. If the dielectric constant is higher than expected at a given location, this could imply that the elevation of the pre-loading surface is overestimated, that additional flexure is required, or that the composition at that local is different (more dust rich) than the rest of the polar cap, and reciprocally. We note that regions where the polar cap is thinnest will be those most sensitive to uncertainties in these quantities. To illustrate how the uncertainty in the denominator of Equation 3 propagates into the estimated dielectric constant, consider the case of a 1 km layer of water ice with $\epsilon' = 3.0$. Using this equation with an uncertainty of ± 100 m for the thickness in the denominator would yield a range of dielectric constants from 2.5 to 3.7 for that layer.

Table 1

Constants Used to Estimate the Composition of the South Polar Deposits (See Broquet et al., 2020; Nunes & Phillips, 2006; Sori & Bramson, 2019; Wiczorek, 2008)

Component	ρ (kg m ⁻³)	ϵ'	Thermal conductivity (W m ⁻¹ K ⁻¹)
H ₂ O ice	920	3.0–3.15	$k(T)^a$
CO ₂ ice	1,560	2.2	0.20–0.75
Dust	2,200–3,400	6.0–8.8	3
CO ₂ -clathrates	1,100	2.85	0.20–0.75

^aThe thermal conductivity of H₂O is determined using the temperature dependent expression of Clifford and Parker (2001).

3. Inversion Results

Before proceeding with the inversion results, it is necessary to define an allowable value of the misfit function in Equation 1. There are several sources of error in the terms of this equation. First, as quantified in the preceding section, there is an uncertainty of about ± 350 m in the height of the pre-loading surface. Superposed on top of the pre-loading surface will be pre-existing topography. For this, we use a value of ± 200 m that corresponds to the terrain roughness of the surrounding highlands at the scale of the first Fresnel zone (~ 23 km). Lastly, we also have an uncertainty of ± 86.5 m for the range resolution of MARSIS in water ice. Assuming that these uncertainties are statistically independent and adding them in quadrature, we obtain a total uncertainty of 412 m.

In the following subsections, we first present the results obtained from MARSIS data where we emphasize that some solutions cannot be simultaneously accounted for by mixtures of ices and dust. Next, we show that additional constraints, including the lack of basal melting beneath the south pole and the observed gravitational attraction of the south polar cap, can be used to restrict the allowed range of parameters. We conclude with a summary of the sensitivity analyses we performed regarding the pre-loading surface, the influence of thick CO₂ deposits (Phillips et al., 2011), or the presence of the Dorsa Argentea Formation (Khuller & Plaut, 2021) on our results.

3.1. MARSIS Constraints and Allowable Mixtures

In Figure 4, we plot the range of acceptable solutions using the misfit function of Equation 1 as a function of T_e , ρ and ϵ' for different scenarios. For these plots, the rms misfit was computed using all MARSIS data picks at the 1,000 locations shown in Figure 2. To facilitate viewing the three-dimensional parameter space, we show the minimum misfit as a function of sets of two parameters. In the left panels, we plot the minimum misfit contour of 412 m, filled in blue. Any solution with a misfit less than this value (in the filled space) is acceptable within the framework of our flexure model and the radar data. As discussed below, we also plot additional independent constraints in the left panels, and the right panels show the restricted range of parameters that fits all considered constraints, where the associated misfit is plotted in color.

We see in Figure 4 (left) that a large range of parameters can fit the data within uncertainties. Our derived 1- σ limits allow for all elastic thicknesses greater than 60 km, with a best-fitting value of 500 km. We note that our inversions did not consider values larger than 500 km as there is little predicted flexure for such values. The range of polar cap densities allows for values from 920 to 2,000 kg m⁻³, with a best-fitting value of 920 kg m⁻³. Our inversions did not consider densities lower and higher than these minimum and maximum values, respectively, as this would correspond to highly implausible compositions for the south polar cap. The range of dielectric constants allows for values between 2.2 and 6.0, with a best-fitting value of 4.1.

Parts of this allowable parameter space corresponds to densities and dielectric constants that cannot be simultaneously obtained by mixtures of ices and dust (see Table 1). The range of solutions that fit the data and that can also be accounted for by a Maxwell-Garnett mixture of these three components are outlined by the purple line in this figure (Sihvola, 2000). We note that the results would be nearly identical (dielectric constant at most 3.5% higher) using a power-law mixing relation as in Nerozzi and Holt (2019) (see also Stillman et al., 2010). Using the permissible mixtures constraint, the allowed parameter space is largely

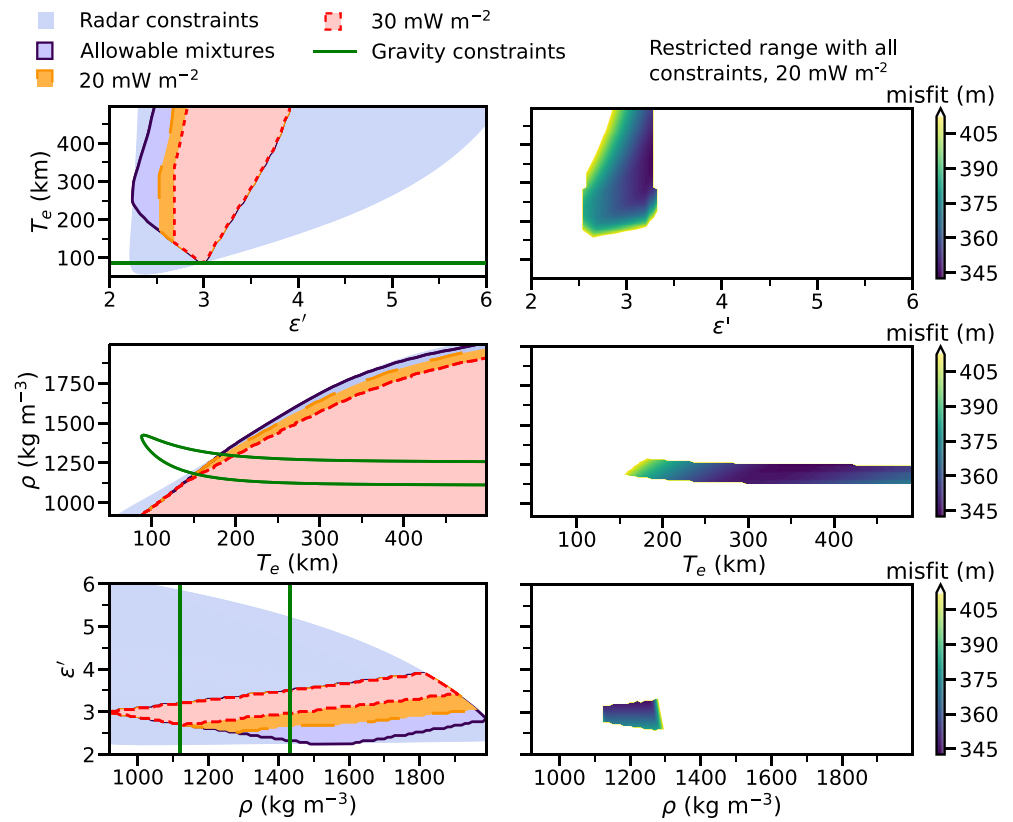


Figure 4. (Left) Filled contours of the parameter space that can fit the observations within uncertainties as a function of the dielectric constant (ϵ'), elastic thickness (T_e), and bulk density of the polar cap (ρ) using Mars Advanced Radar for Subsurface and Ionosphere Sounding data at 1,000 locations. The radar constraints are shown in blue, and the purple lines delimit possible mixtures of real materials. The red and orange lines delimit those same mixtures that do not produce basal melting where the cap is thickest for heat flows of 20 and 30 mW m⁻². The green line shows the allowed parameter space of the independent gravity inversion. (Right) Restricted parameter space using all constraints, and a heat flow of 20 mW m⁻², where the color corresponds to the root-mean-square misfit of Equation 1.

restrained. The range of permissible values for the dielectric constant is reduced to 2.2–3.9 and the minimum elastic thickness increases to 90 km. The range of densities, however, remains unchanged.

3.2. Constraints From Basal Melting

The thermal conductivity of the polar cap is strongly dependent on the relative abundances of ices and dust (Mellon, 1996). If the effective thermal conductivity is low enough, this could result in temperatures that would be sufficient to melt the base of the polar cap. Where the south polar deposits are thickest, basal melting has not been conclusively observed by radar observations, and we thus assume that basal melting is not presently occurring in the innermost regions of the polar cap. Temperature profiles in the polar cap were obtained by solving Fourier's law of heat conduction, assuming a conservative maximum thickness of 4,300 m, and using a three-component Maxwell-Garnett mixing law to compute the thermal conductivity of mixtures (Table 1). The orange and red dashed lines in Figure 4 (left) delimit the allowable parameter space that does not generate basal melting of CO₂ ice (i.e., temperatures less than 216 K) under typical present-day heat flows of 20 and 30 mW m⁻² (Plesa et al., 2018). For a heat flow of 20 mW m⁻², the permissible dielectric constant range decreases somewhat to 2.5–3.9, the elastic thickness range is unmodified by the basal melting constraint, and the range of allowable densities is reduced to 920–1,960 kg m⁻³.

Subglacial liquids were proposed to have been observed beneath the south polar deposits, but only in a 20 km × 30 km region where the polar cap is relatively thin, about 1,400 m thick (Lauro et al., 2020; Orsoi

et al., 2018). Recent MARSIS observations have shown that similar bright reflectors are in fact more widespread throughout the south polar layered deposits than initially thought (Khuller & Plaut, 2021) and do not necessarily require the presence of liquids (Bierson et al., 2021). In order to achieve basal melting locally in these regions, either the local composition would need to be significantly different from the global composition of the south polar cap, or the local heat flow would need to be significantly higher than average (Sori & Bramson, 2019). Given the widespread nature of these bright reflectors, it is unlikely that the atypical temperature conditions required to melt either CO₂ or H₂O ice would exist for all of these regions.

3.3. Constraints From Gravity

Lastly, we considered independent gravity constraints on the density of the south polar cap and the elastic thickness of the underlying lithosphere. These constraints were obtained from an admittance inversion that is nearly identical to that of Wiczorek (2008), but using the more recent gravity model of Genova et al. (2016) (see Figure S7). Based solely on a fit to the observed localized admittance using the theoretical loading model of Broquet and Wiczorek (2019), the best-fitting density was found to be 1,220 kg m⁻³, with an allowable range of 1,110–1,425 kg m⁻³. The best-fit elastic thickness was found to be 171 km, but any elastic thicknesses larger than 90 km was found to fit the gravity data within uncertainties. The range of solutions from this inversion are only slightly different than those presented in Wiczorek (2008), and are plotted in Figure 4 (left) as green contours (middle), and green horizontal (top) and vertical (bottom) lines.

In the right panel of Figure 4, we plot the restricted range of allowed parameters that fit all considered constraints. To compute this restricted range, we included solely those parameters that fit the radar data, that have allowable mixtures, that do not predict basal melting, and that have a density and elastic thickness consistent with the independent gravity constraints. For the lack of basal melting constraint, we used conservatively the lower heat flow of 20 mW m⁻². The colors plotted in the restricted range correspond to the minimum rms misfit of Equation 1 as a function of the two plotted parameters and for any value of the third parameter that satisfies our constraints. When using all constraints, the allowable range of the inversion parameters is significantly restrained. The dielectric constant is found to range from 2.5 to 3.4 with a best-fitting value of 3.3, all elastic thickness greater than 150 km can satisfy the available constraints with a best-fitting value of 360 km, and the density is constrained to lie within the range 1,110–1,300 kg m⁻³ with a best-fitting value of 1,220 kg m⁻³. These results are summarized in Table 2 where they are compared with the values we found previously for the north polar cap using the same inversion technique.

We note that our final inverted range for the bulk density, 1,110–1,300 kg m⁻³, is consistent with that obtained by previous studies that have made various assumptions. Zuber et al. (2007) obtained a 2- σ range of 740–1,780 kg m⁻³ with a best-fit of 1,220 kg m⁻³, Wiczorek (2008) obtained a 1- σ range of 1,166–1,391 kg m⁻³ with a best fit of 1,271 kg m⁻³, and Ding et al. (2019) allowed for all densities lower than 1,400 kg m⁻³, with a best-fit of 1,110 kg m⁻³. Our range for the bulk dielectric constant of 2.5–3.4 is also similar to that assumed in Plaut et al. (2007), 2.5–3.5.

3.4. Sensitivity to the Pre-Loading Surface, CO₂ Deposits, and Dorsa Argentea Formation

In Appendix B, we demonstrate that the pre-loading surface has little impact on the inferred dielectric constant and density of the polar cap. The reason for this is seen in the lower-left panel of Figure 4, which shows that the radar data alone (blue contour) provide only very loose constraints on these parameters. Changing the pre-loading surface within its uncertainties was found to modify the extremities of the blue contour region, but only outside of the final range, we obtain using all constraints. Only the lower limit on the elastic thickness was found to be sensitive to the exact form of the pre-loading surface (see Appendix B).

Thick CO₂ ice deposits are known to exist in regions poleward of 85°S and from longitude 235 to 360°E (Phillips et al., 2011), and these could potentially bias our inversion results. We ran additional inversions excluding this region, and as with our tests that varied the pre-loading surface, the range of parameters allowed solely by the radar data were found to differ only slightly from that shown in Figure 4 (blue fill). The final restricted range for the dielectric constant and density was found to be nearly the same as discussed above, with a best-fitting dielectric constant of 3.4 and a best-fitting density of 1,300 kg m⁻³. The elastic

Table 2

Summary of Results From This Study of the South Polar Cap and That of Broquet et al. (2020) for the North Polar Cap, Which Used a Similar Inversion Method

Parameter	South polar cap	North polar cap
H ₂ O ice (vol%)	40–91	14–100
CO ₂ ice (vol%)	0–60 (15–50 for 6 vol% dust)	0–82 (8–70 for 6 vol% dust)
Dust (vol%)	0–24 (9–18 for no CO ₂)	0–28 (0–5 for no CO ₂)
Density (kg m ⁻³)	1,110–1,300	920–1,520
Dielectric constant	2.50–3.40	2.40–3.15
Elastic thickness (km)	>150	330–450
Maximum flexure (m)	770	400
Surface heat flow (mW m ⁻² , strain of 1)	<28.5	11–16
Surface heat flow (mW m ⁻² , strain of 10 ⁻⁶)	<23.5	10–13
Volume (10 ⁶ km ³)	1.29–2.27	1.31–1.73

Note. Since the dust and CO₂ ice content trades off, we also provide in parentheses the ranges assuming 6 vol% dust and a CO₂-free polar cap. The surface heat flow is given assuming a strain of 1 (i.e., 100%), as in Phillips et al. (2008), and assuming a strain of 10⁻⁶ (Knapmeyer et al., 2006) (see also Figure S10). The assumed loading timescales for the north and south polar caps are 5 and 100 My, respectively.

thickness was found to range from 150 to 485 km, with a best-fitting value of 315 km. Similarly, we have performed an additional inversion that excluded regions poleward of 84°S with longitudes from 95 to 295° E, which correspond to where the Dorsa Argentea Formation is thought to exist (Khuller & Plaut, 2021). The final restricted range for all parameters is nearly identical to that found using all MARSIS data, with a best-fitting dielectric constant of 3.4, a best-fitting elastic thickness of 450 km, and a best-fitting density of 1,300 kg m⁻³.

4. Composition of the South Polar Deposits

To determine the composition of the south polar deposits, we follow the procedure described in Broquet et al. (2020). With this approach, we determine those fractions of H₂O ice, CO₂ ice, and dust that can fit both our bulk density and dielectric constant estimates using all constraints (Figure 4, right). Consistent with the modeling approach described in Section 2, we necessarily assume that the polar unit is homogeneous in composition. In Figure 5, we show a ternary diagram that plots the range of allowable compositions, where the color represents the corresponding dielectric constant (left) and density (right) of the mixture. For this figure, we assume that the dielectric constants of water ice and dust are respectively 3.0 and 6.0, that the density of the dust component is 2,200 kg m⁻³, and that basal melting of CO₂ ice does not occur for a heat flow of 20 mW m⁻².

We find that the south polar deposits are composed mostly of water ice: at least 40 vol% and up to 91 vol% (see Table 2). The CO₂ ice component, however, trades off with the dust concentration. This is easy to understand given that a 1:4 mixture of dust and CO₂ ice has a similar dielectric constant as water ice. We find the CO₂ ice content of the polar cap to lie somewhere between 0 to 60 vol%, and note that it would be at least 28 vol% if the dust content was negligible. A dust-free composition, however, is unlikely as numerous radar observations indicate that the south polar cap is relatively dust-rich (e.g., Plaut et al., 2007; Whitten & Campbell, 2018). If the dust concentration were assumed to be similar to that in the north polar cap (6 vol%, see Broquet et al., 2020; Grima et al., 2009; Nerozzi & Holt, 2019), then the minimum CO₂ ice content would be 15 vol%. Alternatively, if there is negligible CO₂ ice, the dust concentration would lie somewhere between 9 to 18 vol%. We emphasize that the average real dielectric constant is generally between about 3.0 and 3.4 when the CO₂ ice content is less than 20 vol%.

Increasing the dielectric constant of water ice from 3.0 to 3.15 (e.g., Grima et al., 2009; Khuller & Plaut, 2021), or that of the dust from 6.0 to 8.8 (e.g., Nerozzi & Holt, 2019; Nunes & Phillips, 2006), would both exclude

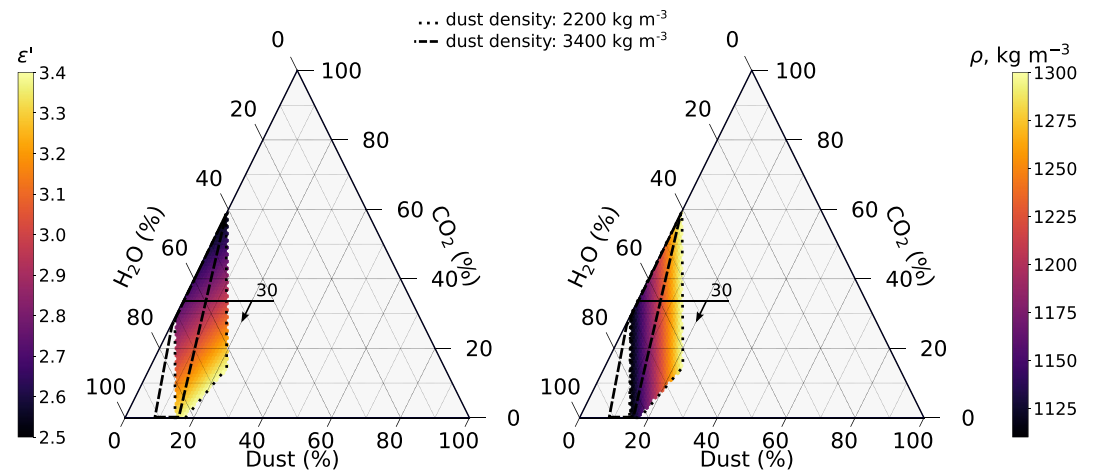


Figure 5. Ternary plots of the allowable volumetric mixtures of water ice, CO₂ ice, and dust, which satisfy the lack of basal melting of CO₂ ice for a heat flow of 20 mW m⁻². The color for each allowable mixture corresponds to the dielectric constant (left) and bulk density (right) using a dust density of 2,200 kg m⁻³. The dielectric constants of water ice and dust were set to 3.0 and 6.0, respectively, and increasing either of these values would increase the minimum allowed CO₂ ice content (Figure S8). The horizontal solid black line limits the regions where basal melting would occur for a higher heat flow of 30 mW m⁻², with acceptable solutions being in the direction given by the black arrow. The dotted and dashed lines delimit the accepted mixtures when the dust density is set to 2,200 and 3,400 kg m⁻³, respectively.

cases where the south polar cap is CO₂-free, and would require a minimum CO₂ ice content of about 10 vol% (see Figure S8). For a heat flow at the south pole of 30 mW m⁻², the maximum amount of CO₂ ice in these cases can be limited to about 36 vol% (as opposed to a maximum of 62 vol% for a heat flow to 20 mW m⁻²). Using a lower thermal conductivity for CO₂ ice of 0.2 W m⁻¹ K⁻¹ as in Sori and Bramson (2019) would further limit the maximum amount of CO₂ ice to about 48 and 25 vol% for heat flows of 20 and 30 mW m⁻², respectively.

We ran additional models where we replaced CO₂ ice with CO₂-clathrates. In this case, both the maximum water and dust abundance remained nearly the same at 92 vol%, and 24 vol%, respectively, but the concentration of the clathrates was found to be entirely unconstrained (Figure S9). We note that having a large concentration of clathrates in the polar deposits is unlikely since they form at high pressure and in the presence of CO₂ (e.g., Stewart & Nimmo, 2002).

5. Surface Heat Flow in the South Polar Region

The present-day temperature gradient beneath a polar cap, and hence heat flow, can be constrained if the total amount of lithospheric flexure beneath the polar cap is known (Table 2). In Broquet et al. (2020), we made use of the formalism developed in McNutt (1984) to infer the north polar surface heat flow based on the estimated elastic thickness of the lithosphere, lithospheric curvature, and for an assumed strain rate and internal rheology. In that study, the strain rate was assumed to be 10⁻¹⁴ s⁻¹, the same as in Phillips et al. (2008), which is the inverse of the north polar cap formation timescale. Furthermore, we used a wet diabase rheology for the crust and a dry olivine rheology for the mantle, a low bounding stress of 10 MPa, and a thermal conductivity of respectively 3 and 4 W m⁻¹ K⁻¹ for the crust and mantle (see also Balta & McSween, 2013; Phillips et al., 2008; Plesa et al., 2018). For an elastic thickness of 330 km, and for the case where there is no heat production in the crust, the surface heat flow (which is the same as the mantle heat flow) was found to be 12 mW m⁻². When including a crustal heat production based on Gamma-ray spectroscopy analyses of the Martian surface (about 5 mW m⁻², Hahn et al., 2011), the mantle heat flow was found to be 1 mW m⁻² lower (see also Ruiz et al., 2006), and the surface heat flow increased to about 16 mW m⁻². For

the upper limit elastic thickness of 450 km and when crustal heat production was considered, the mantle and surface heat flows were computed to be 6 and 11 mW m^{-2} , respectively.

For the south pole, we use similar parameters, but test different strain rates (Table 2, Figure S10). Using an estimated age of the south polar cap of 100 Ma (Koutnik et al., 2002) and the approach of Phillips et al. (2008), where the strain rate is approximated as the inverse of the polar cap age, we obtain a strain rate of about 10^{-16} s^{-1} . When including crustal heat production (about 8.5 mW m^{-2} , Hahn et al., 2011) and for elastic thicknesses greater than 150 km, the surface and mantle heat flows are computed to be less than 28.5 and 20 mW m^{-2} , respectively. Given that we were not able to obtain an upper bound for the elastic thickness in our study, heat flows as low as zero are allowable given the uncertainties in the data. We note that our upper limit for the surface heat flow of 28.5 mW m^{-2} is consistent with the present-day values obtained in the thermal evolution simulations of Plesa et al. (2018) at the south pole that are about $28 \pm 5 \text{ mW m}^{-2}$.

Approximating the strain rate as the inverse of the polar cap age, however, assumes that there is 100% strain over the age of the polar cap, which is unrealistically high given the small amount of deformation underneath the polar cap. Assuming a more appropriate lower strain of 10^{-6} as computed from observed faults (e.g., Knapmeyer et al., 2006), the strain rate could be as low as 10^{-22} s^{-1} . For comparison, we note that strain rates of 10^{-17} s^{-1} are typically used for large-scale loads associated with the Martian volcanoes (McGovern et al., 2002). For this case, and if the elastic thickness is greater than 150 km, the surface and mantle heat flows are found to be less than 23.5 and 15 mW m^{-2} , respectively. Based on these considerations, we reassess the heat flow estimate underneath the north polar cap from Broquet et al. (2020). If a strain of 10^{-6} is assumed for the north pole (instead of 100%), a strain rate of 10^{-20} s^{-1} would be obtained using a polar cap age of 5 Ma. When accounting for crustal heat production, the surface and mantle heat flows are predicted to be 10–13 mW m^{-2} and 5–8 mW m^{-2} , respectively, which are only marginally lower than our previous estimates (see Table 2).

In a study by Ojha et al. (2021), the authors made use of a maximum possible 1-km downwarping of the lithosphere beneath the south polar cap to infer the maximum local mantle heat flow. This constraint was based on a preliminary estimate of less than 500 m of deflection from radar analyses by Plaut et al. (2007), along with an additional 500 m of uncertainty resulting from potential variations in the dielectric constant. In this study, we predict a maximum flexure beneath the south polar cap of 770 m that is smaller than, though still consistent with, that used in Ojha et al. (2021). Although both studies use somewhat similar constraints, Ojha et al. (2021) made use of a more detailed elasto-viscoplastic deformation model, and determined that the mantle heat flow at the base of the lithosphere should be less than 10 mW m^{-2} . Their upper limit lies in the range of possible solutions we find in this study, which is a mantle heat flow of less than 15 mW m^{-2} .

Even though these two mantle heat flow estimates are mutually consistent, we note that there are several factors that could influence their upper limits. First, we could have overestimated the unknown strain rate associated with the deformation at the south pole. For example, in order to obtain mantle heat flows as low as 10 mW m^{-2} for an elastic thickness of 150 km, the strain rate at the south pole would have to be lower than 10^{-26} s^{-1} (Figure S10), implying strains of less than 10^{-10} . These strains would be orders of magnitude lower than typical Martian contractional strains of 10^{-4} to 10^{-6} (Andrews-Hanna et al., 2008; Knapmeyer et al., 2006). Another possibility is that Ojha et al. (2021) overestimated the total stress of the polar cap acting on the lithosphere, as a result of their using a simple one-dimensional axisymmetric stress profile for the load, when the polar cap is in fact highly non-axisymmetric. As an example, if the stress were 25% lower, a mantle heat flow of about 13 mW m^{-2} would be accepted, which would be closer to our estimate. Finally, the thickness of the crust is a crucial parameter in elasto-viscoplastic deformation modeling, as the crust is significantly weaker than the mantle, but this parameter was not varied in Ojha et al. (2021). A thinner crust in their models for the south pole would allow for higher mantle heat flows.

6. Conclusions

We have used MARSIS data, constraints on allowable mixtures, the absence of basal melting, and gravity and topography data to probe the composition of the south polar cap of Mars and the present-day elastic thickness of the underlying lithosphere. Our results show that the 1- σ limits on the bulk density of the south polar cap range from 1,110 to 1,300 kg m⁻³ (with a best-fit of 1,220 kg m⁻³), the dielectric constant ranges from 2.5 to 3.4 (with a best-fit of 3.3), and the elastic thickness of the lithosphere is larger than 150 km (with a best-fit of 360 km). Using the formalism of McNutt (1984), the lower bound on the elastic thickness can be shown to imply a surface heat flow lower than 23.5 mW m⁻² and a mantle heat flow less than 15 mW m⁻² in the south polar region. Although there are significant uncertainties associated with the estimation of the surface elevation before the polar cap formed, our sensitivity analyses have shown that the density and dielectric constant (and hence our inferred compositions) are mostly insensitive to the shape of the pre-loading surface.

The minimum elastic thickness allowed from our inversion (150 km), is considerably thinner than the allowable range we found previously for the north pole, which is 330–450 km (Broquet et al., 2020). Though the two elastic thickness ranges do overlap, thermal evolution models of Mars that consider lateral variations in crustal thickness generally predict higher surface heat flows (and hence lower elastic thicknesses) in the southern highlands than in the northern lowlands (e.g., Grott & Breuer, 2010; Knapmeyer-Endrun et al., 2021; Plesa et al., 2018; Thiriet et al., 2018). The origin of this difference is related simply to a higher total crustal heat production for the thick crust in the southern highlands relative to the thinner crust in the northern lowlands, combined with differences in the resulting thermal insulation of the underlying mantle from the crustal thickness variations. Based on a large suite of thermal evolution simulations with different initial conditions, Plesa et al. (2018) predicted very few cases where the elastic thickness is the same in the two hemispheres. Whereas elastic thicknesses of about 200–600 km were allowed in the north in their study, for the south, this range was limited to only about 50–300 km (Plesa et al., 2018). Thus, even though our analysis obtains only a minimum allowable elastic thickness of 150 km beneath the south polar cap, when combined with our results for the north pole, these values are entirely consistent with the predicted expected hemispheric differences in the present-day heat flow of Mars. We emphasize that elastic thicknesses greater than 300 km in the southern highlands would, in fact, be difficult to reconcile with what is known of the thermal evolution of Mars.

In our simulations, the maximum allowed central deflection of the lithosphere is 770 m, giving a maximum polar cap thickness of about 3,900 m. We predict a maximum flexural signature that is less than 200 and 100 m at the edge of the cap and equatorward of 75°S, respectively, and that would be likely too small to be detected in the elevation of the rough southern highlands. Integrating the polar cap thickness and the maximum predicted flexure gives a 1- σ upper limit for the total volume of the polar deposits of 2.27×10^6 km³, which is about 26% higher than the 1- σ upper limit of Plaut et al. (2007) that did not include any lithospheric deflection. This could represent a significant quantity of trapped volatiles that are not accounted for by studies that establish the inventory of available volatile reservoirs on Mars (e.g., Jakosky & Edwards, 2018).

Assuming that the south polar cap is made of a mixture of dust, water ice, and CO₂ ice, we determined the allowable range of compositions. Similar to the north polar cap, the principal component of the south polar deposits is water ice, which given the uncertainties of our analysis can range from 40 to 91 vol%. The quantity of CO₂ is poorly constrained and trades off with the abundance of dust. The entire allowable range is from 0% to 60%, but much of this range is improbably high given that thick mapped CO₂ deposits are thought to represent only a minor fraction of the south polar deposits (e.g., Phillips et al., 2011). If there is at most 1% CO₂ in the south polar cap, as initially mapped by Phillips et al. (2011) (see also Bierson et al., 2016; Putzig et al., 2018), we infer that the bulk dust content is at least 9 vol%, and up to 18 vol%, which is larger than what we previously found at the north pole (less than 5 vol% for no CO₂). Higher dust contents in the south polar cap, in comparison to the north polar cap, could potentially be the reason why SHARAD is only able to see clearly through the uppermost 1 km of the south polar deposits (Whitten & Campbell, 2018), as the instrument has a shallow penetration depth in dust-rich layers (Nunes & Phillips, 2006; Seu et al., 2007). Although compositions with negligible CO₂ ice are permitted, the CO₂ ice content would be at least 15 vol% if we assume a dust content similar to that in the north polar cap of about 6 vol% (see Broquet et al., 2020; Nerozzi & Holt, 2019). Increasing our nominal values for the dielectric constant of water ice or dust, or

adding more dust to the polar cap, would require an even larger solid CO₂ content (Figure S8). For most of our inferred south polar cap compositions, the bulk dielectric constant of the mixture is generally larger than 3.0 (up to 3.4) when the CO₂ ice content is less than about 20 vol%.

We note that estimated radar depths of the polar cap basal surface, which assume a bulk dielectric constant lower than the true value, would generate fictitious short-wavelength relief that is anti-correlated with the surface topography. Lithospheric flexure also generates a deflection that is anti-correlated with the surface topography, but only at long-wavelengths comparable to the size of the polar cap. If these two signals could be isolated, it might be possible to improve upon the results presented in this work, and hence decrease the range of acceptable solutions. The horizontal spacing of the radar picks in our analysis was ~15 km, which allows us to adequately investigate the long-wavelength shape of the surface beneath the south polar cap, but not the shortest wavelengths. A high-resolution map of the south polar cap basement, with a spacing of about 1.5 km, was recently made available by Khuller and Plaut (2021), and this data set could help to provide constraints on the dielectric constant based on the inferred variations in short-wavelength basal relief. We note that the south polar cap likely has both long-wavelength and short-wavelength variations in composition (hence in dielectric constant), and that this would complicate such analyses.

For reasonable dust contents (6–9 vol%), our study suggests, but does not require, that there could be up to 15 times more CO₂ ice than previous estimated in the south polar cap. These mixtures, as well as those in Broquet et al. (2020) have a dielectric constant of about 3 and higher and would not generate basal relief anti-correlated with the surface topography, in contrast to what was suggested by Ojha et al. (2021). If such a larger quantity of CO₂ ice in fact exists, in order not to be detectable as radar reflections, it would be required to be in the form of thin layers, with a thickness less than several times the SHARAD and MARSIS resolutions (a few meters, see Lalich & Holt, 2017). These deposits could further be hidden from mapping analyses if they were discontinuous or intimately mixed with water ice. Such scenarios are not implausible as every winter, the south polar cap is covered by a meter scale layer of CO₂ (Murray et al., 1972). If covered by dust or water ice, the CO₂ deposits could in some cases be thermally insulated during the southern summer and subsequently buried (Bierson et al., 2016; Manning et al., 2019). An independent estimate on the dust concentration within the south polar cap, such as with radar reflectivity (Lalich et al., 2019), would help to place crucial constraints on the volume of sequestered CO₂ ice in the deposits.

Appendix A: Non-Detectability of a Flexure Signal Exterior of the South Polar Cap

The models presented in Section 3 predict up to about 200 m of lithospheric flexure at the edge of the south polar cap. In this appendix, we show that this flexural signal is unlikely to be visible in the rugged highlands surrounding the south polar cap. In particular, we (a) generate synthetic topographic models that have the same spectral characteristics as the surrounding highlands, (b) compute one-dimensional topographic profiles averaged over longitude, and (c) compare the synthetic one-dimensional profiles with the flexural signals predicted for several allowable elastic thicknesses.

We started by computing the power spectrum of the surface relief, localized to a region in the rugged southern highlands, using a localized spectral analysis technique (Wieczorek & Simons, 2005, 2007). In generating the localized power spectrum, we employed a single localization window that was designed to concentrate more than 99% of its energy in a spherical cap with an angular radius of 45°. The spherical harmonic bandwidth of this window (l_{win}) is 5, and for the topography model itself, we used the degree 2,600 model of Wieczorek (2015). We centered the window over the south pole, but note that the exact location of the window had little impact on the obtained power spectrum. We further note that the localized power spectrum using a window with an angular radius of 60° is nearly identical to that using a radius of 45°. In order to avoid those portions of the resulting localized spectrum that could be biased by the localization procedure (Wieczorek & Simons, 2005, 2007), we considered spherical harmonic degrees greater than $3 \times l_{win}$ and less than $2600 - l_{win}$ (the coefficients outside of this range were set to zero). For reference, the extent of the south polar cap corresponds to a spherical harmonic of about degree 8.

With this estimate of the power spectrum of the rugged highlands, we generated synthetic spherical harmonic coefficients for the global topography of Mars. The value for each individual coefficient was obtained

from a Gaussian distribution, with the degree-dependent standard deviation being chosen to satisfy the observed localized power spectrum. For each realization of this stochastic process, we generated a grid of the synthetic topography from the spherical harmonic coefficients, averaged the resulting topography over longitude, and then plotted the one-dimensional profile from the average edge of the polar cap (700 km distance) to 2,000 km distance from the south pole. We note that the south polar cap is highly asymmetric and that it extends in places to about 71°S, which is a distance of about 1,100 km from the south pole. Hundred such realizations are plotted in the upper panel of Figure A1, and a single representative profile is highlighted in blue.

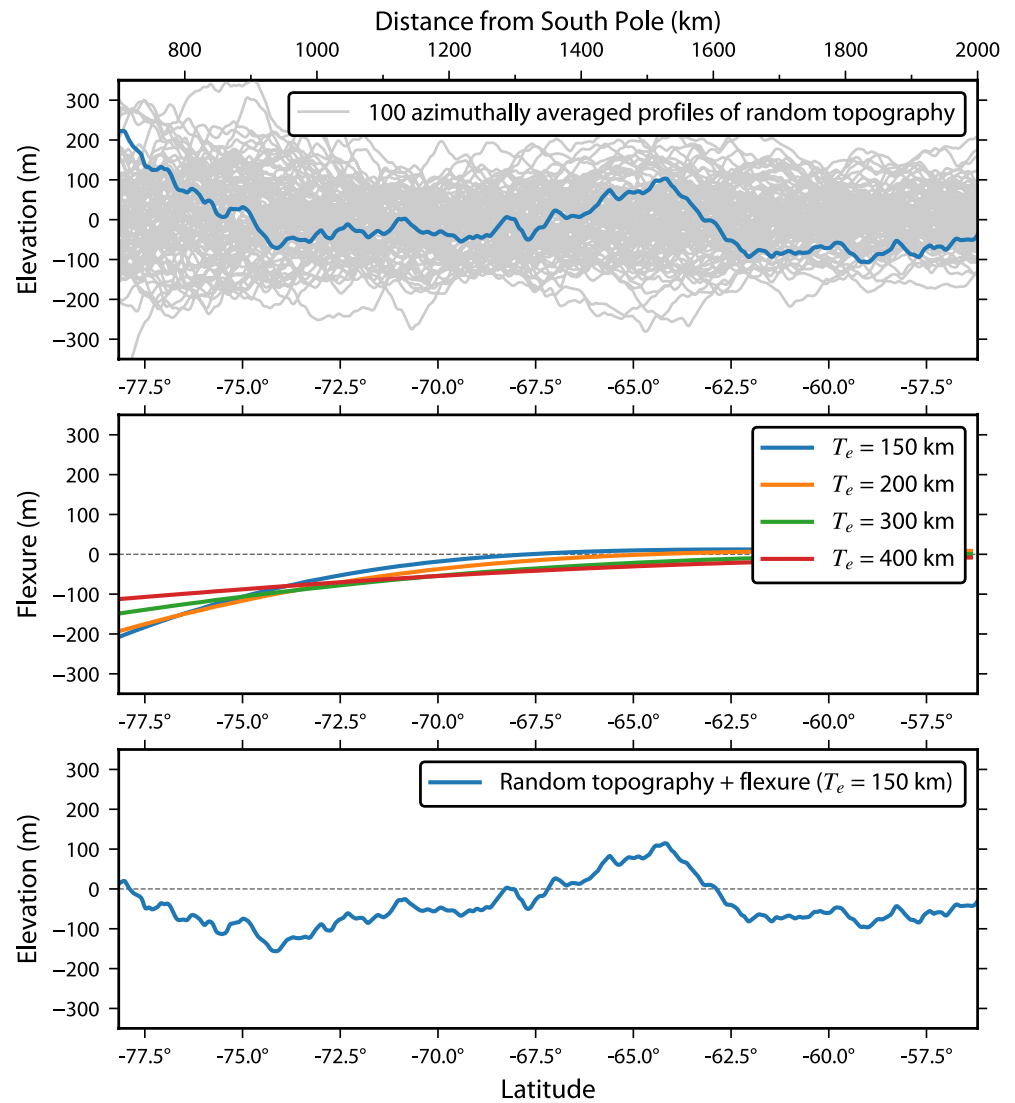


Figure A1. Demonstration showing that the natural variability of surface relief in the southern highlands is comparable to the expected flexural signal of the south polar cap. (Upper) Hundred azimuthally averaged profiles of simulated Martian surface relief, plotted from the average edge of the polar cap (700 km) to 2,000 km distance from the south pole. A representative profile is highlighted in blue. (Middle) Simulated flexure profiles for assumed elastic thicknesses ranging from 150 to 400 km. (Bottom) Predicted surface relief when combining the flexural profile using an elastic thickness of 150 km and the blue profile in the upper panel. The original flexure signal is unrecognizable.

We emphasize that these profiles are unmodified when the spherical harmonic coefficients are filtered to exclude the highest spherical harmonic degrees: this is because the act of averaging over longitude already filters out the shortest wavelength signals. We note that the standard deviation of the profiles is about 90 m. This standard deviation is likely to be an underestimate of the true variability given that we excluded spherical harmonic degrees less than 15, and given that the power spectrum of planetary topography usually increases with decreasing degree. Furthermore, the spherical harmonic coefficients of the true global topography are not in reality statistically independent and uncorrelated as assumed. Any departure from these idealistic assumptions would likely increase the variability of our azimuthally averaged topographic profiles.

In the middle panel of Figure A1, we plot the predicted flexural profiles exterior of the south polar cap for elastic thicknesses of 150, 200, 300 and 400 km. We note that the maximum lithospheric deflection is about 200 m at the average edge of the polar cap for the lowest elastic thickness. Beyond 1,000 km from the pole (or 300 km from the average edge of the polar cap), the predicted deflection is less than 100 m for all elastic thicknesses. We further note that the flexural bulge has an amplitude of only 12 m for our lowest elastic thickness. In the lower panel of this figure, we add the blue profile in the upper panel to the predicted flexural profile for an elastic thickness of 150 km. As this plot shows, it is not possible to discern the original flexural signal when considering the natural statistical variations that are expected in the surrounding highlands.

Lastly, we computed the slopes of our one-dimensional azimuthally averaged profiles and compared these with the observed slope. Given that the south polar cap extends in places to about 71°S, we computed the slope from 60 to 71°S as was done in the main text. The average slope was found to be close to zero, and the standard deviation of the distribution was found to be 12 m per degree latitude. By definition, there is a 68% chance (i.e., $1-\sigma$) that the absolute value of the slope will be less than 12 m per degree and a 95% chance (i.e., $2-\sigma$) that the slope will be less than 24 m per degree. We note that positive and negative slopes are equally probable. The standard deviation of the slope of 12 m per degree compares favorably with, though is somewhat lower than, the observed slope of about 20 m per degree latitude. Nevertheless, for the same reasons as described above, it is likely that our estimated standard deviation of the slope is an underestimate given that it was computed using an idealistic stochastic process. In any case, the observed slope is certainly consistent with the 95% confidence limits of the synthetic slope distribution.

As a final remark, we note there are additional sources that could contribute to hiding a flexural signal. For example, it is possible that the flexural moat could have been partially filled by polar cap derived deposits. As an example, if the south polar cap has 5 to 10 vol% dust, this would correspond to an equivalent layer of about 50–100 m. If the polar cap retreated in size and deposited all this material on the surface (as was suggested for the origin of the Dorsa Argentea Formation that surrounds the south polar cap, see Whitten et al., 2020), this could hide a significant portion of the existing flexural signal. Viscoelastic relaxation effects and post-glacial rebound could also complicate the identification of a flexural signal. The polar caps form on geologically short timescales (Levrard et al., 2007) and it is possible that at some point the extent of the south polar unit was larger (see Rodriguez et al., 2015). The disappearance of that load would cause a slow viscous uplift of the south polar terrains that would compete with and slow-down the present-day flexural signature associated with the load of the current polar cap. This could generate a zero net (or even positive) flexural signal at the edge of the polar cap. Lastly, we note that some of the models shown in the study of Ojha et al. (2021) do in fact predict zero flexure outside of the south polar cap when the crustal heat contribution is large, but this was not investigated in detail in that paper.

Appendix B: Uncertainty of the Pre-Loading Surface and Its Influence on the Inversion Parameters

In Broquet et al. (2020), elevation data equatorward of 75°N (about 900 km away from the north pole) were used to find the best-fitting pre-loading surface beneath the north polar cap. At such distances, the predicted deflection is less than 50 m and does not bias the interpolated elevation beneath the polar cap. In that study, a conservative uncertainty of 170 m was associated with the estimated pre-loading surface, and was obtained by comparing pre-loading surfaces obtained using various masking procedures. In this appendix,

we determine the uncertainty associated with the pre-loading surface beneath the south polar cap, and investigate its influence on the density and dielectric constant of the polar deposits, and the elastic thickness of the lithosphere.

The southern terrains show relief variations on the order of 2 km over tens of kilometer length scale, and it was difficult to define a mask based on a latitudinal band as was done for the north polar cap. In order to limit the contribution of the rugged surface topography in the southern highlands, we tested several methods for estimating the pre-loading surface. We have shown an estimate of the pre-loading surface in Figure 2 that was obtained by interpolating surface elevations poleward from the edge of the south polar cap as defined by Tanaka et al. (2014). In the upper row of Figure S1, we show two possible additional pre-loading surfaces obtained using the average topography within two different latitudinal bands. In one image, we used the average value between 65.5°S and 70.5°S, whereas in the other we used the average value between 67.5°S and 72.5°. For these two cases, the pre-loading surface was found to be on average 520 and 600 m below that shown in Figure 2. In the lower row of this image, we used the same latitude bands, but instead determined the best-fitting linear function in latitude and extrapolated toward the pole. For these two cases, the pre-loading surface was found to be on average 180 and 230 m below that shown in Figure 2. For both cases, the height of the pre-loading surface is opposite of what one would expect for a flexural signal associated with the polar cap.

For our third technique, as shown in Figure S2, we constructed a mask of the polar deposits where we attempted to avoid spurious topographic signals, while remaining somewhat close to the geologic mapping of Tanaka et al. (2014). The pre-loading surface was then obtained using data equatorward of this boundary and the minimum curvature method of Smith and Wessel (1990) assuming a tension of 0.35, which is recommended for steep topography. For this technique, the average elevation of the pre-loading surface was found to be about 300 m below that used in Figure 2, which is again the opposite of what one would expect for a flexural signal.

For our fourth and last technique, we estimated the flexure at the edge of the polar cap, which is located at 700 km from the south pole on average, using an elastic thickness of 90 km. This elastic thickness is the minimum value allowed from our gravity inversion that do not make use of the radar constraints (as discussed in Section 3 and Figure S7). We note that this elastic thickness is 10 km lower than the minimum estimate of Wiczorek (2008), and that it is considerably less than our minimum accepted value of 150 km when radar constraints are considered. The amount of flexure for this model is thus larger than what we expect. The maximum predicted flexure that could arise at the average edge of the south polar cap is found to be about 350 m (Figure S3), and the average pre-loading surface should hence be 350 m above the average elevation of the edge of the polar cap. Based on these four scenarios, we will assume that the elevation of the pre-loading surface is inherently uncertain by ± 350 m. This value will be used when estimating the uncertainty of the model inversion parameters in the main text.

We performed additional inversions using the pre-loading surfaces shown in Figures S1 and S2. We here report the range of solutions that fit the radar and gravity constraints, and that can also be accounted for by a Maxwell-Garnett mixture of dust, water ice, and CO₂ ice, as in the main text. Using each of the four pre-loading surfaces shown in Figure S1, we obtained compositional results that were consistent with those of the main text, with dielectric constants ranging from 2.5 to 3.8 (2.5–3.4 in the main text) and densities ranging from 1,110 to 1,300 kg m⁻³ (identical to the main text). Only the lower limit of the elastic thickness varied significantly from 200 to 350 km (150 km in the main text). Using the pre-loading surface shown in Figure S2 (left), the dielectric constant was found to range from 2.5 to 3.4 (identical to the main text), and the polar cap density was found to lie between 1,110 and 1,260 kg m⁻³ (1,110–1,300 kg m⁻³ in the main text). The minimum elastic thickness was found to be 300 km, which is larger, but not inconsistent with that of the main text.

Lastly, we performed a test where we added 350 m, everywhere to the pre-loading surface of Figure 2. Three hundred and fifty meters are the maximum predicted flexure that could arise at the edge of the south polar cap for an elastic thickness of 90 km and load density of 1,300 kg m⁻³ (Figure S3). For this inversion, the dielectric constant was found to range from 2.5 to 4.0 (2.5–3.4 in the main text), and the density was found to lie between 1,165 and 1,420 kg m⁻³ (1,110–1,300 kg m⁻³ in the main text). The minimum elastic thickness was found to be equal to 90 km (150 km in the main text), which was the value used to estimate the value of

350 m deflection at the edge of the polar cap. Estimates for the dielectric constant and density are consistent with the results shown in the main text. Though the lower bound of the elastic thickness was found to differ modestly from that in the main text, as mentioned above, the assumed 350 m of flexure was derived from the lowest possible elastic thickness from an independent gravity inversion that did not incorporate any radar constraints. It is thus very likely that this test greatly overestimated the amount of lithospheric flexure.

These tests show that our results for the inverted dielectric constant and density are largely independent of the details of the assumed pre-loading surface. As it is these two parameters that determine the composition of the polar cap, our inverted compositions are thus not affected significantly by the choice of the pre-loading surface. Only the inverted elastic thickness was found to be affected by the pre-loading surface.

Appendix C: Elastic Loading Model

The elastic loading model used in this study is based on Broquet and Wiczorek (2019), Broquet et al. (2020), and can be found at Broquet (2021a). Since the load depends explicitly upon the deflection (w) and the density (ρ), we first define the load thickness from MOLA surface elevations and the initial pre-loading surface ($h_e - h_0$), and then iterate by adding the amount of corresponding deflected materials to the load. Typically, only a few iterations are necessary to converge to sub-meter accuracies.

The governing equation relating the support mechanism that links a load q and w has been derived by Kraus (1967). This equation can be written as

$$\left[D(\nabla^2 + 2)^3 - 2D(\nabla^2 + 2)^2 + ET_e R_e^2 (\nabla^2 + 2) \right] w(\theta, \phi) = -R_e^4 (\nabla^2 + 1 - \nu) q(\theta, \phi), \quad (C1)$$

where, θ and ϕ are the colatitude and longitude, respectively. $D = ET_e^3 / 12(1 - \nu^2)$, is the flexural rigidity of the shell, and R_e is the radius of the elastic shell, taken to be its midpoint, $R_e = R - T_e / 2$. The load q is defined to be positive when directed downward, whereas deflections are considered to be positive when measured upward. By expressing the load and deflection in spherical harmonics as q_{lm} and w_{lm} , and using the identity of the Laplacian in the spectral domain, $\nabla^2 Y_{lm} = -l(l+1)Y_{lm}$, the equation of Kraus (1967) can be written in linear form as (Turcotte et al., 1981)

$$w_{lm} = \xi^l q_{lm} = -\frac{R_e^4 [l(l+1) - 1 + \nu]}{Dn^3 + 2Dn^2 + ET_e R_e^2 n} q_{lm}, \quad (C2)$$

with $n = l(l+1) - 2$.

The total load acting on the lithosphere can be shown to be equal to (e.g., Broquet & Wiczorek, 2019)

$$q_{lm} = w_{lm} (\Delta\rho_l g_0 + \Delta\rho_c g_m) + \rho_l g_0 h_{lm}^s - \Delta\rho_c U_{lm}(R - T_c) - \rho_c U_{lm}(R). \quad (C3)$$

Here, $\Delta\rho_l = \rho_c - \rho_l$, $\Delta\rho_c = \rho_m - \rho_c$, g_0 and g_m are the vertical gravitational acceleration at the surface and at the crust-mantle boundary, and h_{lm}^s is the surface topography. In this equation, the first term corresponds to the deflection of the lithosphere into the fluid mantle (an Archimedean force), the second to the weight of the load, and the two last to a small correction due to changes to the gravitational potential (U_{lm}) induced by the load and deflection (i.e., “self-gravity”).

Using the mass-sheet approximation, where $\bar{\rho}$ is the mean planetary density, the potential at the surface and at the base of the crust resulting from deflections of each density interface is given by

$$U_{lm}(R) = \frac{3g_0}{\bar{\rho}(2l+1)} \left[\rho_l h_{lm}^s + \Delta\rho_l w_{lm} + \Delta\rho_c w_{lm} \left(\frac{R - T_c}{R} \right)^{l+2} \right], \quad (C4)$$

$$U_{lm}(R - T_c) = \frac{3g_0}{\bar{\rho}(2l+1)} \left[\left(\rho_l h_{lm}^s + \Delta\rho_l w_{lm} \right) \left(\frac{R - T_c}{R} \right)^l + \Delta\rho_c w_{lm} \left(\frac{R - T_c}{R} \right) \right]. \quad (C5)$$

Inserting Equations C3–C5 into Equation C2 yields, after some algebra

$$w_{lm} = -\frac{\rho_l \bar{C}_l^s}{\Delta\rho_c} h_{lm}^s, \quad (C6)$$

where, for $\varphi = (R - T_c) / R$,

$$\bar{C}_l^s = \frac{1 - \frac{3}{\bar{\rho}(2l+1)} [\rho_c + \Delta\rho_c \varphi^l]}{\frac{g_m}{g_0} + \frac{\Delta\rho_l}{\Delta\rho_c} - \frac{1}{\xi^l g_0 \Delta\rho_c} - \frac{3}{\bar{\rho}(2l+1)} \left[\Delta\rho_l \varphi^l + \Delta\rho_c \varphi + \rho_c \left(\frac{\Delta\rho_l}{\Delta\rho_c} + \varphi^{l+2} \right) \right]}. \quad (C7)$$

Data Availability Statement

Python routines to compute the flexure and heat flow are available at Broquet (2021a, 2021b), respectively. The spherical harmonic model of the gravity field is available at Zuber et al. (2010) and that of the topography from Wieczorek (2015). The reduced radar data used in this study are available on the Planetary Data System Geosciences Node website at <https://pds-geosciences.wustl.edu/> or on the Planetary Science Archive of the European Space Agency website at <https://www.cosmos.esa.int/web/psa/mars-express>. The radar and MOLA-based thicknesses plotted in Figure 2 can be accessed at Broquet et al. (2021). The ternary plot was made using the python-ternary package of Harper et al. (2015). Most of the color maps used in this manuscript are from Crameri (2018).

Acknowledgments

The authors thank the editor Laurent Montsi and two anonymous reviewers for providing helpful comments on the manuscript. W. Fa is supported by Beijing Municipal Science and Technology Commission (Z191100004319001) and National Key Research and Development project (2019YFE0123300), and the contribution of M. Wieczorek is supported by the French Space Agency (CNES).

References

- Andrews-Hanna, J. C., Zuber, M. T., & Hauck, S. A., II. (2008). Strike-slip faults on Mars: Observations and implications for global tectonics and geodynamics. *Journal of Geophysical Research*, *113*(E8). <https://doi.org/10.1029/2007JE002980>
- Balta, J. B., & McSween, J. H. Y. (2013). Water and the composition of Martian magmas. *Geology*, *41*(10), 1115–1118. <https://doi.org/10.1130/G34714.1>
- Bierson, C. J., Phillips, R. J., Smith, I. B., Wood, S. E., Putzig, N. E., Nunes, D., & Byrne, S. (2016). Stratigraphy and evolution of the buried CO₂ deposit in the Martian south polar cap. *Geophysical Research Letters*, *43*(9), 4172–4179. <https://doi.org/10.1002/2016GL068457>
- Bierson, C. J., Tulaczyk, S., Courville, S. W., & Putzig, N. E. (2021). Strong MARSIS radar reflections from the base of Martian south polar cap may be due to conductive ice or minerals. *Geophysical Research Letters*, *48*. <https://doi.org/10.1029/2021GL093880>
- Broquet, A. (2021a). *AB-Ares/Displacement_strain_planet: Version 0.2.3*. Zenodo. <https://doi.org/10.5281/zenodo.5075617>
- Broquet, A. (2021b). *AB-Ares/Te_HF_Conversion: Version 0.1.0*. Zenodo. <https://doi.org/10.5281/zenodo.4922606>
- Broquet, A., & Wieczorek, M. A. (2019). The gravitational signature of Martian volcanoes. *Journal of Geophysical Research: Planets*, *124*(8), 2054–2086. <https://doi.org/10.1029/2019JE005959>
- Broquet, A., Wieczorek, M. A., & Fa, W. (2020). Flexure of the lithosphere beneath the north polar cap of Mars: Implications for ice composition and heat flow. *Geophysical Research Letters*, *47*(5). <https://doi.org/10.1029/2019GL086746>
- Broquet, A., Wieczorek, M. A., & Fa, W. (2021). *The composition of the south polar cap of Mars derived from orbital data*. Zenodo. <https://doi.org/10.5281/zenodo.468298310.1029/2020je006730>
- Clifford, S. M., & Parker, T. J. (2001). The evolution of the Martian hydrosphere: Implications for the fate of a primordial ocean and the current state of the northern plains. *Icarus*, *154*(1), 40–79. <https://doi.org/10.1006/icar.2001.6671>
- Crameri, F. (2018). *Scientific colour maps: Perceptually uniform and colour-vision deficiency friendly*. Zenodo. <https://doi.org/10.5281/zenodo.1243862>
- Ding, M., Lin, J., Gu, C., Huang, Q., & Zuber, M. T. (2019). Variations in Martian lithospheric strength based on gravity/topography analysis. *Journal of Geophysical Research: Planets*, *124*, 3095–3118. <https://doi.org/10.1029/2019JE005937>
- Genova, A., Goossens, S., Lemoine, F. G., Mazarico, E., Neumann, G. A., Smith, D. E., & Zuber, M. T. (2016). Seasonal and static gravity field of Mars from MGS, Mars Odyssey and MRO radio science. *Icarus*, *272*, 228–245. <https://doi.org/10.1016/j.icarus.2016.02.050>
- Goossens, S., Sabaka, T. J., Genova, A., Mazarico, E., Nicholas, J. B., & Neumann, G. A. (2017). Evidence for a low bulk crustal density for Mars from gravity and topography. *Geophysical Research Letters*, *44*(15), 7686–7694. <https://doi.org/10.1002/2017GL074172>
- Grima, C., Kofman, W., Mougnot, J., Phillips, R. J., Hérique, A., Biccari, D., et al. (2009). North polar deposits of Mars: Extreme purity of the water ice. *Geophysical Research Letters*, *36*, L03203. <https://doi.org/10.1029/2008GL036326>
- Grott, M., & Breuer, D. (2010). On the spatial variability of the Martian elastic lithosphere thickness: Evidence for mantle plumes? *Journal of Geophysical Research*, *115*, E03005. <https://doi.org/10.1029/2009JE003456>
- Hahn, B. C., McLennan, S. M., & Klein, E. C. (2011). Martian surface heat production and crustal heat flow from Mars Odyssey Gamma-Ray spectrometry. *Geophysical Research Letters*, *38*(14). <https://doi.org/10.1029/2011GL047435>
- Harper, M., Weinstein, B., Simon, S., chebee7i, Swanson-Hysell, N., Badger, T. G., et al. (2015). *Python-ternary: Ternary plots in python*. Zenodo. <https://doi.org/10.5281/zenodo.34938>
- Herkenhoff, K. E., & Plaut, J. J. (2000). Surface ages and resurfacing rates of the polar layered deposits on Mars. *Icarus*, *144*(2), 243–253. <https://doi.org/10.1006/icar.1999.6287>
- Jakosky, B. M., & Edwards, C. S. (2018). Inventory of CO₂ available for terraforming Mars. *Nature Astronomy*, *2*, 634–639. <https://doi.org/10.1038/s41550-018-0529-6>

- Khuller, A. R., & Plaut, J. J. (2021). Characteristics of the basal interface of the Martian south polar layered deposits. *Geophysical Research Letters*, *48*. <https://doi.org/10.1029/2021GL093631>
- Knappmeyer-Endrun, B., Panning, M. P., Bissig, F., Joshi, R., Khan, A., Kim, D., et al. (2021). Thickness and structure of the Martian crust from InSight seismic data. *Science*, *373*(6553), 438–443. <https://doi.org/10.1126/science.abf8966>
- Knappmeyer, M., Oberst, J., Hauber, E., Whlisch, M., Deuchler, C., & Wagner, R. (2006). Working models for spatial distribution and level of Mars' seismicity. *Journal of Geophysical Research*, *111*(E11). <https://doi.org/10.1029/2006JE002708>
- Koutnik, M., Byrne, S., & Murray, B. (2002). South polar layered deposits of Mars: The cratering record. *Journal of Geophysical Research*, *107*(E11), 5100. <https://doi.org/10.1029/2001JE001805>
- Kraus, H. (1967). *Thin elastic shells: An introduction to the theoretical foundations and the analysis of their static and dynamic behavior* (p. 467). John Wiley.
- Lalich, D. E., & Holt, J. W. (2017). New Martian climate constraints from radar reflectivity within the north polar layered deposits. *Geophysical Research Letters*, *44*(2), 657–664. <https://doi.org/10.1002/2016GL071323>
- Lalich, D. E., Holt, J. W., & Smith, I. B. (2019). Radar reflectivity as a proxy for the dust content of individual layers in the Martian north polar layered deposits. *Journal of Geophysical Research: Planets*, *124*(7), 1690–1703. <https://doi.org/10.1029/2018JE005787>
- Laskar, J., Levrard, B., & Mustard, J. (2002). Orbital forcing of the Martian polar layered deposits. *Nature*, *419*, 375–377. <https://doi.org/10.1038/nature01066>
- Lauro, S. E., Pettinelli, E., Caprarelli, G., Guallini, L., Rossi, A. P., Mattei, E., et al. (2020). Multiple subglacial water bodies below the south pole of Mars unveiled by new MARSIS data. *Nature Astronomy*, *5*, 63–70. <https://doi.org/10.1038/s41550-020-1200-6>
- Levrard, B., Forget, F., Montmessin, F., & Laskar, J. (2007). Recent formation and evolution of northern Martian polar layered deposits as inferred from a global climate model. *Journal of Geophysical Research: Planets*, *112*(E6). <https://doi.org/10.1016/10.1029/2006JE002772>
- Lorius, C., Jouzel, J., Ritz, C., Merlivat, L., Barkov, N. I., Korotkevich, Y. S., & Kotlyakov, V. M. (1985). A 150,000-year climatic record from Antarctic ice. *Nature*, *316*, 591–596. <https://doi.org/10.1038/316591a0>
- Manning, C. V., Bierson, C., Putzig, N. E., & McKay, C. P. (2019). The formation and stability of buried polar CO₂ deposits on Mars. *Icarus*, *317*, 509–517. <https://doi.org/10.1016/j.icarus.2018.07.021>
- McGovern, P. J., Solomon, S. C., Smith, D. E., Zuber, M. T., Simons, M., Wieczorek, M. A., et al. (2002). Localized gravity/topography admittance and correlation spectra on Mars: Implications for regional and global evolution. *Journal of Geophysical Research*, *107*(E12). <https://doi.org/10.1029/2002JE001854>
- McNutt, M. K. (1984). Lithospheric flexure and thermal anomalies. *Journal of Geophysical Research*, *89*(B13), 180–194. <https://doi.org/10.1029/JB089iB13p11180>
- Mellon, M. T. (1996). Limits on the CO₂ content of the Martian polar deposits. *Icarus*, *124*(1), 268–279. <https://doi.org/10.1006/icar.1996.0203>
- Murray, B. C., Soderblom, L. A., Cutts, J. A., Sharp, R. P., Milton, D. J., & Leighton, R. B. (1972). Geological framework of the south polar region of Mars. *Icarus*, *17*(2), 328–345. [https://doi.org/10.1016/0019-1035\(72\)90004-8](https://doi.org/10.1016/0019-1035(72)90004-8)
- Nerozzi, S., & Holt, J. (2019). Buried ice and sand caps at the north pole of Mars: Revealing a record of climate change in the Cavi unit with SHARAD. *Geophysical Research Letters*, *46*, 7278–7286. <https://doi.org/10.1029/2019GL082114>
- Neumann, G. A., Zuber, M. T., Wieczorek, M. A., McGovern, P. J., Lemoine, F. G., & Smith, D. E. (2004). Crustal structure of Mars from gravity and topography. *Journal of Geophysical Research*, *109*(E8). <https://doi.org/10.1029/2004JE002262>
- Nunes, D. C., & Phillips, R. J. (2006). Radar subsurface mapping of the polar layered deposits on Mars. *Journal of Geophysical Research*, *111*(E6). <https://doi.org/10.1029/2005JE002609>
- Ojha, L., Karimi, S., Buffo, J., Nerozzi, S., Holt, J. W., Smrekar, S., & Chevrier, V. (2021). Martian mantle heat flow estimate from the lack of lithospheric flexure in the south pole of Mars: Implications for planetary evolution and basal melting. *Geophysical Research Letters*, *48*(2). <https://doi.org/10.1029/2020GL091409>
- Ojha, L., Nerozzi, S., & Lewis, K. (2019). Compositional constraints on the north polar cap of Mars from gravity and topography. *Geophysical Research Letters*, *46*, 8671–8679. <https://doi.org/10.1029/2019GL082294>
- Orosei, R., Jordan, R., Morgan, D., Cartacci, M., Cicchetti, A., Duru, F., et al. (2015). Mars Advanced Radar for Subsurface and Ionospheric Sounding (MARSIS) after nine years of operation: A summary. *Planetary and Space Science*, *112*, 98–114. <https://doi.org/10.1016/j.pss.2014.07.010>
- Orosei, R., Lauro, S. E., Pettinelli, E., Cicchetti, A., Coradini, M., Cosciotti, B., et al. (2018). Radar evidence of subglacial liquid water on Mars. *Science*, *361*(6401), 490–493. <https://doi.org/10.1126/science.aar7268>
- Phillips, R. J., Davis, B. J., Tanaka, K. L., Byrne, S., Mellon, M. T., Putzig, N. E., et al. (2011). Massive CO₂ ice deposits sequestered in the south polar layered deposits of Mars. *Science*, *332*(6031), 838–841. <https://doi.org/10.1126/science.1203091>
- Phillips, R. J., Zuber, M. T., Smrekar, S. E., Mellon, M. T., Head, J. W., Tanaka, K. L., et al. (2008). Mars north polar deposits: Stratigraphy, age, and geodynamical response. *Science*, *320*(5880), 1182–1185. <https://doi.org/10.1126/science.1157546>
- Picardi, G., Plaut, J. J., Biccari, D., Bombaci, O., Calabrese, D., Cartacci, M., et al. (2005). Radar soundings of the subsurface of Mars. *Science*, *310*(5756), 1925–1928. <https://doi.org/10.1126/science.1122165>
- Plaut, J. J., Picardi, G., Safaeinili, A., Ivanov, A. B., Milkovich, S. M., Cicchetti, A., et al. (2007). Subsurface radar sounding of the south polar layered deposits of Mars. *Science*, *316*(5821), 92–95. <https://doi.org/10.1126/science.1139672>
- Plesa, A.-C., Padovan, S., Tosi, N., Breuer, D., Grott, M., Wieczorek, M. A., et al. (2018). The thermal state and interior structure of Mars. *Geophysical Research Letters*, *45*(22), 12198–12209. <https://doi.org/10.1029/2018GL080728>
- Putzig, N. E., Smith, I. B., Perry, M. R., Foss, F. J., Campbell, B. A., Phillips, R. J., & Seu, R. (2018). Three-dimensional radar imaging of structures and craters in the Martian polar caps. *Icarus*, *308*, 138–147. <https://doi.org/10.1016/j.icarus.2017.09.023>
- Rodriguez, J. A. P., Leonard, G. J., Platz, T., Tanaka, K. L., Kargel, J. S., Fairn, A. G., et al. (2015). New insights into the late Amazonian zonal shrinkage of the Martian south polar plateau. *Icarus*, *248*, 407–411. <https://doi.org/10.1016/j.icarus.2014.08.047>
- Ruiz, J., McGovern, P. J., & Tejero, R. (2006). The early thermal and magnetic state of the cratered highlands of Mars. *Earth and Planetary Science Letters*, *241*(1), 2–10. <https://doi.org/10.1016/j.epsl.2005.10.016>
- Selvans, M. M., Plaut, J. J., Aharonson, O., & Safaeinili, A. (2010). Internal structure of Planum Boreum, from Mars Advanced Radar for Subsurface and Ionospheric Sounding data. *Journal of Geophysical Research*, *115*(E9). <https://doi.org/10.1029/2009JE003537>
- Seu, R., Phillips, R. J., Alberti, G., Biccari, D., Bonaventura, F., Bortone, M., et al. (2007). Accumulation and erosion of Mars' south polar layered deposits. *Science*, *317*(5845), 1715–1718. <https://doi.org/10.1126/science.1144120>
- Sihvola, A. (2000). Mixing rules with complex dielectric coefficients. *Subsurface Sensing Technologies and Applications*, *1*(4), 393–415. <https://doi.org/10.1023/A:1026511515005>

- Smith, W. H. F., & Wessel, P. (1990). Gridding with continuous curvature splines in tension. *Geophysics*, *55*(3), 293–305. <https://doi.org/10.1190/1.1442837>
- Sori, M. M., & Bramson, A. M. (2019). Water on Mars, with a grain of salt: Local heat anomalies are required for basal melting of ice at the south pole today. *Geophysical Research Letters*, *46*(3), 1222–1231. <https://doi.org/10.1029/2018GL080985>
- Stewart, S. T., & Nimmo, F. (2002). Surface runoff features on Mars: Testing the carbon dioxide formation hypothesis. *Journal of Geophysical Research*, *107*(E9), 7-1–7-12. <https://doi.org/10.1029/2000JE001465>
- Stillman, D. E., Grimm, R. E., & Dec, S. F. (2010). Low-frequency electrical properties of ice-silicate mixtures. *The Journal of Physical Chemistry B*, *114*(18), 6065–6073. <https://doi.org/10.1021/jp9070778>
- Tanaka, K. L., Skinner, J. A. J., Dohm, J. M., Irwin, R. P. I., Kolb, E. J., Fortezzo, C. M., et al. (2014). *Geologic map of Mars* (U.S. Geological Survey Scientific Investigations Map 3292, Scale 1:20,000,000. Pamphlet, 43). <https://doi.org/10.3133/sim3292>
- Thiriet, M., Michaut, C., Breuer, D., & Plesa, A.-C. (2018). Hemispheric dichotomy in lithosphere thickness on Mars caused by differences in crustal structure and composition. *Journal of Geophysical Research: Planets*, *123*(4), 823–848. <https://doi.org/10.1002/2017JE005431>
- Turcotte, D. L., Willemann, R. J., Haxby, W. F., & Norberry, J. (1981). Role of membrane stresses in the support of planetary topography. *Journal of Geophysical Research*, *86*(B5), 3951–3959. <https://doi.org/10.1029/JB086iB05p03951>
- Whitten, J. L., & Campbell, B. A. (2018). Lateral continuity of layering in the Mars south polar layered deposits from SHARAD sounding data. *Journal of Geophysical Research: Planets*, *123*(6), 1541–1554. <https://doi.org/10.1029/2018JE005578>
- Whitten, J. L., Campbell, B. A., & Plaut, J. J. (2020). The ice content of the Dorsa Argentea Formation from radar sounder data. *Geophysical Research Letters*, *47*(23). <https://doi.org/10.1029/2020GL090705>
- Wieczorek, M. A. (2008). Constraints on the composition of the Martian south polar cap from gravity and topography. *Icarus*, *196*, 506–517. <https://doi.org/10.1016/j.Icarus.2007.10.026>
- Wieczorek, M. A. (2015). Gravity and topography of the terrestrial planets. In *Treatise on geophysics* (pp. 153–193). <https://doi.org/10.1016/B978-0-444-53802-4.00169-X>
- Wieczorek, M. A., & Simons, F. J. (2005). Localized spectral analysis on the sphere. *Geophysical Journal International*, *162*, 655–675. <https://doi.org/10.1111/j.1365-246X.2005.02687.x>
- Wieczorek, M. A., & Simons, F. J. (2007). Minimum-variance multitaper spectral estimation on the sphere. *Journal of Fourier Analysis and Applications*, *13*(6), 665–692. <https://doi.org/10.1007/s00041-006-6904-1>
- Zuber, M. T., Konopliv, A., & Lemoine, F. G. (2010). *MRO radio science derived gravity science data products v1.0*. NASA Planetary Data System. <https://doi.org/10.17189/1519521>
- Zuber, M. T., Phillips, R. J., Andrews-Hanna, J. C., Asmar, S. W., Konopliv, A. S., Lemoine, F. G., et al. (2007). Density of Mars' south polar layered deposits. *Science*, *317*(5845), 1718–1719. <https://doi.org/10.1126/science.1146995>